

# Morphology Development, Structure and Dielectric Properties of Biaxially Oriented Polypropylene

Ilkka Rytöluoto<sup>1</sup>, Mikael Ritamäki<sup>1</sup>, Antonis Gitsas<sup>2</sup>, Satu Pasanen<sup>3</sup> & Kari Lahti<sup>1</sup>

<sup>1</sup>Tampere University of Technology, Laboratory of Electrical Energy Engineering, Finland

<sup>2</sup>Borealis Polyolefine GmbH, Innovation & Technology, Austria

<sup>3</sup>VTT Technical Research Centre of Finland, Finland

## Abstract

This paper outlines our recent study on effects of cast film extrusion and biaxial orientation on the morphological development and dielectric performance of biaxially oriented polypropylene (PP) films based on two capacitor-grade isotactic PP (iPP) raw materials. Results on polymorphic composition, melting behavior, microstructure and dielectric properties are reported. Morphological development during film manufacturing is found to have a profound effect on film structure and dielectric characteristics. Formation of structural defects was traced back to  $\beta \rightarrow \alpha$  crystal transformation upon biaxial stretching.

## 1. Introduction

Biaxially oriented isotactic polypropylene (BOPP) film produced by tenter frame process is the current state-of-the-art dielectric medium in both oil-impregnated film-foil capacitors and metallized film (dry) capacitors. BOPP film exhibits superior dielectric strength (small-area breakdown strength of  $\sim 700$  V/ $\mu\text{m}$ ), very low dielectric loss ( $\tan \delta \sim 10^{-4}$ ) and excellent self-healing dielectric breakdown capability in metallized film capacitors [1]. While these properties arise essentially from the weakly polar nature and high purity of commercially available capacitor-grade PP resins, the film structure and morphology also play a very important role in determining the mechanical, thermal and dielectric properties of BOPP. For instance, biaxial stretching and the associated transformation of the spherulitic cast film morphology into highly oriented fibrillar morphology [2] is generally known to be one of the main contributing factors for the superior dielectric strength of capacitor-grade BOPP [3]. The structural and morphological development during BOPP film manufacturing is in turn largely dictated by the processing parameters used in cast film manufacturing and biaxial stretching [4]. However, surprisingly few systematic studies have been published on the dependence of dielectric properties on the base PP properties, film processing parameters and the resulting morphology—such knowledge would provide further means to optimize dielectric performance of BOPP capacitor films.

This paper outlines our recent study [5] on processing–structure–dielectric property relationships of two capacitor-grade isotactic PP (iPP) materials which were

extruded into 200–500  $\mu\text{m}$  cast films using three different extruders and subsequently biaxially oriented using a laboratory sheet stretching machine with two different stretch-ratios to produce BOPP films in the 10–15  $\mu\text{m}$  thickness range. Extensive material characterization was performed for the cast and biaxially oriented film samples, including: (i) crystalline structure, (ii) melting behavior, (iii) surface roughness, haze, orientation and cross-sectional structure, (iv) large-area DC dielectric breakdown performance, and (v) permittivity and dielectric loss. The observed correlations between film morphology, structure and dielectric properties are outlined, emphasizing the dielectric property dependence on the precursor (cast) film  $\beta$ -form crystallinity,  $\beta \rightarrow \alpha$  crystal transformation and subsequent void/porosity formation upon biaxial stretching. This paper extends the above structure–property analysis by introducing supportive differential scanning calorimetry, dielectric spectroscopy and small-area dielectric breakdown data.

## 2. Experimental

### 2.1. Materials and film processing

Material specifications and film processing parameters are presented in Table 1. Two capacitor-grade iPP homopolymers were used, PP1 (Borclean™ HB311BF) and PP2 (Borclean™ HC300BF), out of which PP2 is of high isotacticity grade. The polymers, obtained in the form of stabilized pellets, were dried at 70 °C overnight and thereafter extruded into cast films with minimum machine directional (MD) orientation. In order to study the effect of cast film extrusion process and equipment on the film morphology and dielectric performance, three different extruders were utilized for the cast film manufacturing. The extruders differed mainly in terms of machine size and most importantly in processing parameters, i.e. cylinder temperature profile, die temperature and chill roll temperature, see Table 1. The cast extrusion parameters affected the melt crystallization conditions as will be discussed later on. Specimens cut from the cast films were simultaneously biaxially stretched by using a Brückner Maschinenbau KARO IV laboratory stretching machine. Equibiaxial stretch-ratios of either  $3.5 \times 3.5$  (200  $\mu\text{m}$  cast films) or  $5.6 \times 5.6$  (400–500  $\mu\text{m}$  cast films) were used. The resulting BOPP films were  $\sim 10$ –15  $\mu\text{m}$  in thickness. The naming convention of the samples is: [polypropylene type] – [extruder] – [cast film thickness] – [stretch-ratio] (if biaxially oriented).

## 2.2. Material characterization

Wide-angle X-ray scattering (WAXS) measurements were performed to determine crystallinity and polymorphic composition of both the cast and biaxially oriented films. The diffraction measurements were carried out in reflection geometry by a Bruker Discover D8 diffractometer with Ni-filtered  $\text{CuK}\alpha$  X-rays (wavelength  $\lambda = 1.5418 \text{ \AA}$ ). The X-ray diffraction data were treated by first subtracting amorphous halo from the diffraction profiles and then using a multi-peak fitting procedure to fit the remaining crystalline peaks. Turner-Jones  $\beta$ -form crystal index ( $k_\beta$ ), a widely used relative measure of the  $\beta$ -crystalline content, was calculated in accordance with the literature [6]. WAXS degree of crystallinity,  $X_{\text{WAXS}}$ , was calculated by dividing the area under the crystalline curve by the total area under the original spectrum.

Differential scanning calorimetry (DSC) measurements were performed on cast and biaxially stretched film specimens using a TA Instruments Q2000 DSC. The DSC was calibrated frequently using an indium standard and the measurements were performed under a constant nitrogen gas purge of 50 ml/min. The samples ( $6.2 \pm 0.6 \text{ mg}$  and  $2.6 \pm 0.2 \text{ mg}$  for the cast film and BOPP film samples, respectively) were heated from  $0 \text{ }^\circ\text{C}$  to  $220 \text{ }^\circ\text{C}$  at  $10 \text{ }^\circ\text{C}/\text{min}$ , maintained isothermally for 5 min and then cooled to  $0 \text{ }^\circ\text{C}$  at  $10 \text{ }^\circ\text{C}/\text{min}$ . Melting enthalpy ( $\Delta H_f$ ), onset of melting ( $T_{\text{om}}$ ) and melting temperature ( $T_m$ ) were determined from the first heating curves to study the initial morphologies. Crystallization temperature ( $T_c$ ) was determined from the subsequent cooling run. DSC degree of crystallinity ( $X_{\text{DSC}}$ ) was calculated from  $\Delta H_f$  using the value of  $\Delta H_\alpha^0 = 209 \text{ g/J}$  for the heat of fusion of a completely crystalline  $\alpha$ -form iPP material [7].

Surface and cross-sectional morphologies of the cast films and biaxially stretched films were studied by optical microscopy (OM), scanning electron microscopy (SEM) and 3D optical profiling. OM analysis was carried out by using a Meiji Techno ML8530 microscope equipped with a polarizing facility and a digital camera. Thin cast film sections for the OM analysis were prepared using a Microm HM 325 microtome at room temperature and imaged under cross-polarized reflected light. SEM analysis was performed on Au-sputtered samples by using a Tescan VEGA3 SB scanning electron

microscope. SEM cross-sectional analysis of the biaxially stretched films was performed on specimens broken in liquid nitrogen. Optical profilometry was carried out by using a Veeco Wyko® NT1100 optical profiling system in vertical scanning interferometry (VSI) mode. Surface roughness statistics were calculated using the open-source Gwyddion software

## 2.2. Dielectric characterization

Dielectric spectroscopy measurements were performed on both cast and biaxially stretched film specimens using a Novocontrol Alpha-A dielectric analyzer and a shielded BDS-1200 sample cell at room temperature under a test voltage of  $1 \text{ V}_{\text{RMS}}$ . Electrodes were prepared in accordance with the IEC-60250 standard. For the cast films, Al-foil electrodes ( $\varnothing 40 \text{ mm}$ ) were applied to both sides of the specimen using a minuscule amount of low-dielectric-loss silicone grease (Molykote® 111 compound). For the BOPP films, Au-electrodes ( $\varnothing 12 \text{ mm}$ ) approximately 50 nm in thickness were deposited on both sides of the specimen using a Leybold L560E e-beam evaporator.

DC dielectric breakdown characteristics of the biaxially oriented films were analyzed by (i) large-area self-healing breakdown measurement approach and (ii) small-area single-breakdown measurement approach. The large-area multi-breakdown measurement and data analysis have been detailed in e.g. [8], [9]. The advantage of the self-healing multi-breakdown approach is the ability to acquire a statistically large amount of breakdown data from a relatively large total film area in a bottom-up manner by utilizing a progressive voltage ramp test. The active area in the large-area multi-breakdown measurement was  $81 \text{ cm}^2$  per sample and six samples in total were measured. The small-area single-breakdown measurements were performed in accordance with IEC-60243 standard using the methodology detailed in [8]. The active area in the small-area single-breakdown measurement was  $1 \text{ cm}^2$  and 20 samples in total were measured. For the sake of brevity, further details on the DC breakdown measurements are omitted from this paper. For the statistical analysis of breakdown data, either single 2-parameter (2-p) Weibull distribution or, if necessary, additively mixed 2-p Weibull distribution was utilized [8], [9].

**Table 1** – Cast and biaxially stretched film specifications.  $T_{\text{cylinder}}$  is the extruder cylinder temperature profile,  $T_{\text{die}}$  is the die temperature,  $T_{\text{cr}}$  is the chill roll temperature,  $d_{\text{cast}}$  is the mean cast film thickness,  $t_{\text{pre}}$  is the pre-heating time prior to biaxial stretching,  $T_{\text{set}}$  is the biaxial stretching (set) temperature and  $d_{\text{BOPP}}$  is the mean BOPP film thickness. Extruders A: Brabender Plasticorder (small-scale single-screw extruder), B: Dolci 1 (large-scale single-screw extruder) and C: Barmag (small-scale single-screw extruder).

Code	PP	Cast film manufacturing						Biaxial orientation			
		Extruder	$T_{\text{cylinder}}$ ( $^\circ\text{C}$ )	$T_{\text{die}}$ ( $^\circ\text{C}$ )	$T_{\text{cr}}$ ( $^\circ\text{C}$ )	$d_{\text{cast}}$ ( $\mu\text{m}$ )	$t_{\text{pre}}$ (s)	$T_{\text{set}}$ ( $^\circ\text{C}$ )	Stretch-ratio	$d_{\text{BOPP}}$ ( $\mu\text{m}$ )	
PP1-A-500-5.6	PP1	A	220–230–230–230	230	90	499	120	157	$5.6 \times 5.6$	15.6	
PP1-B-400-5.6	PP1	B	160–195–220–230	230	88	409	120	157	$5.6 \times 5.6$	12.5	
PP1-C-400-5.6	PP1	C	220–230–260–260	270	80	413	120	157	$5.6 \times 5.6$	13.4	
PP1-C-200-3.5	PP1	C	220–230–260–260	270	80	199	100	157	$3.5 \times 3.5$	13.4	
PP2-A-500-5.6	PP2	A	220–230–230–230	230	90	481	120	157	$5.6 \times 5.6$	15.2	
PP2-B-400-5.6	PP2	B	160–195–220–230	230	88	404	120	157	$5.6 \times 5.6$	12.1	
PP2-C-400-5.6	PP2	C	220–230–260–260	270	80	401	120	157	$5.6 \times 5.6$	12.6	
PP2-C-200-3.5	PP2	C	220–230–260–260	270	80	198	100	157	$3.5 \times 3.5$	12.3	

Sample film thicknesses for the dielectric spectroscopy and breakdown strength measurement were determined at multiple points using a high-precision thickness measurement gauge (LE1000-1) to ensure accuracy in relative permittivity and breakdown field calculation. For multi-breakdown data, breakdown fields were calculated event-by-event by rigorously determining average thickness around each self-healed breakdown spot by means of the video recording and the sample film thickness map in MATLAB [8], [9].

### 3. Results and discussion

#### 3.2. Morphology and film structure

##### Morphology

Figure 1a presents DSC first heating endotherms of the iPP cast films reflecting the extruded film morphology. For each cast film, a major melting peak characteristic to  $\alpha$ -form iPP was observed in the  $\sim 163$ – $165$  °C region

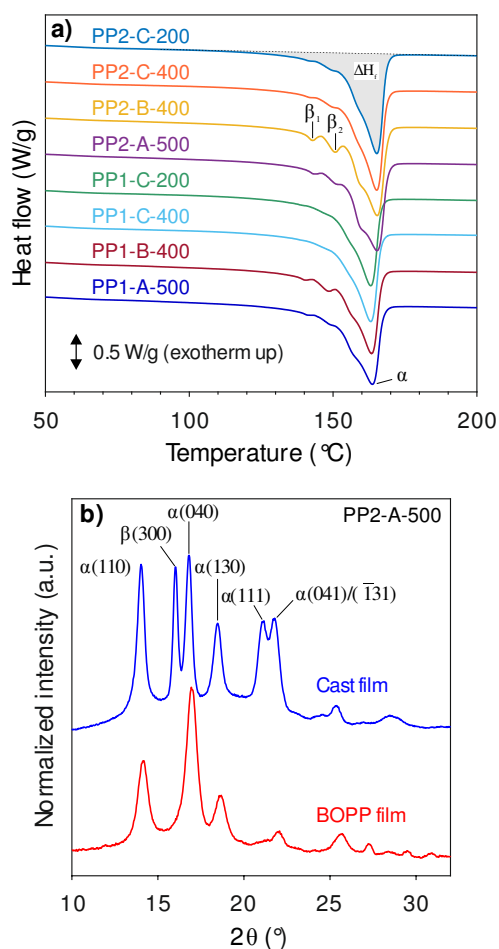


**Figure 1** – **a)** DSC first heating scans of the cast films. Melting peaks corresponding to  $\alpha$ - and  $\beta$ -form crystallinity are labeled. Calculation of  $\Delta H_f$  was based on a linear baseline between 90 °C and the end of melting. The curves are shifted vertically for clarity. **b)** Exemplifying WAXS diffraction profiles of PP2-A-500 cast film and PP2-A-500-5.6 BOPP film. Main diffraction peaks characteristic to monoclinic  $\alpha$ -form and hexagonal  $\beta$ -form crystals are labeled. The curves are normalized and shifted vertically for clarity.

(Table 2), with the high-isotacticity PP2-based cast films showing  $T_m$  ( $\alpha$ ) higher than that of PP1. Additionally, double  $\beta$  peaks in the form of  $\beta_1$  and  $\beta_2$  peaks were observed for the cast films below the major  $\alpha$ -melting peak at  $\sim 142$  °C and  $\sim 150$  °C, respectively—this result is in accordance with Offord et al. [6], [10] and is typical for  $\beta$ -form iPP crystallized both isothermally and non-isothermally below 125 °C. The double  $\beta$  melting behavior reflects melting of the original  $\beta_1$ -phase and subsequent recrystallization into more stable  $\beta_2$ -phase during the DSC heating scan. The formation of  $\beta$ -form crystallinity upon melt extrusion of iPP is known to be dictated by the cooling gradient induced upon cast film extrusion (i.e. extrusion temperature and chill roll temperature, see Table 1), with a faster crystallization rate resulting in thermodynamically less favorable conditions for  $\beta$ -form crystal growth [4]. This explains the differences seen in double  $\beta$  peak intensities between extruders A, B and C (Figure 1a), indicating differences in  $\beta$ -form crystal content for the cast films.

Exemplifying WAXS diffraction profiles of a PP2-A-500 cast film and a biaxially stretched PP2-A-500-5.6 film are presented in Figure 1b. The cast film WAXS diffraction profile confirms the polymorphic  $\alpha/\beta$  crystalline structure seen in DSC scans—the cast films were predominantly of monoclinic  $\alpha$ -form but also showed varying amounts of hexagonal  $\beta$ -form crystallinity, as identifiable by the characteristic reflection at  $2\theta$  angle of  $16.1^\circ$  corresponding to  $\beta(300)$  crystallographic plane. The relative  $\beta$ -form crystal indices ( $k_\beta$ ) enlisted in Table 2 indicate that the cast films manufactured by Extruder B exhibited the highest  $\beta$ -crystallinity. A slightly higher tendency for PP2 to form  $\beta$ -form crystals during cast film manufacturing is also noticed from Table 2, similarly as in [11]. Cast film WAXS crystallinity indices (not shown) were in the range of 67–71 %, which, albeit being higher than those determined from the DSC scans ( $X_{DSC} = 46 \pm 2$  %), are in relative agreement with the DSC analysis.

The WAXS profile of the PP2-A-500-5.6 BOPP film specimen shown in Figure 1b indicates almost complete disappearance of  $\beta$ -form crystallinity upon biaxial stretching, as indicated by the major reduction of  $\beta(300)$  diffraction intensity. This was also confirmed by the disappearance of  $\beta$  melting peaks in the DSC scans of the BOPP films (not shown). The observed behavior can be attributed to a strain-induced  $\beta \rightarrow \alpha$  crystal transformation upon biaxial stretching of iPP cast film in a partly molten

**Table 2** – Cast film properties from DSC and WAXS measurements.

Code	$k_\beta$	$\Delta H_f$ (J/g)	$X_{DSC}$ (%)	$T_m(\beta_1)$ (°C)	$T_m(\beta_2)$ (°C)	$T_m(\alpha)$ (°C)	$T_c$ (°C)
PP1-A-500	0.15	92.9	44.5	141.0	148.3	163.6	114.4
PP1-B-400	0.25	92.6	44.3	140.0	148.4	163.4	114.7
PP1-C-400	0.13	91.7	43.9	141.2	149.6	163.2	114.1
PP1-C-200	0.09	92.2	44.1	141.6	149.8	163.0	114.7
PP2-A-500	0.26	102.3	48.9	143.0	150.7	165.3	117.0
PP2-B-400	0.34	101.1	48.4	142.8	150.6	165.4	117.2
PP2-C-400	0.10	98.9	47.3	141.8	149.7	165.2	117.0
PP2-C-200	0.15	99.7	47.7	141.3	149.3	165.3	117.1

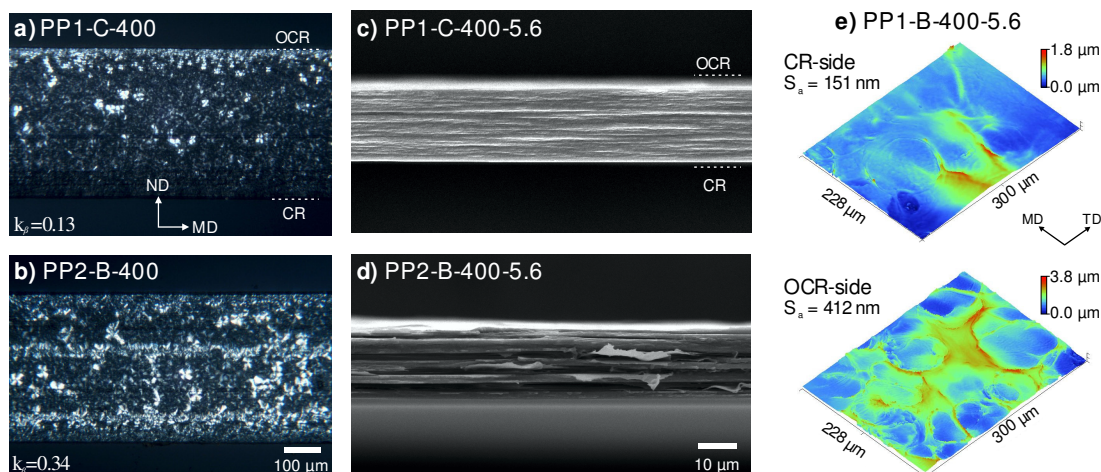


**Figure 2 – a) & b)** Cross-sectional OM images of cast film specimens under cross-polarized reflected light for PP1-C-400 and PP2-B-400 cast films, respectively. **c) & d)** SEM cross-sectional micrographs of cryo-broken PP1-C-400-5.6 and PP2-B-400-5.6 BOPP film specimens, respectively. **e)** Optical profilometer height profile of a PP1-B-400-5.6 BOPP film specimen. Chill roll side (CR), opposite side of chill roll (OCR), normal direction (ND), machine direction (MD) and transverse direction (TD) are labeled. In e),  $S_a$  is the mean area surface roughness.

state [6], [12]. Moreover, changes in the  $\alpha$ -form diffraction peak intensities upon biaxial stretching (Figure 1b) indicate alignment of crystallites as discussed elsewhere [12], [13]. No pronounced differences in degree of crystallinity upon biaxial stretching was detected ( $X_{WAXS} = 68 \pm 1\%$  and  $X_{DSC} = 52 \pm 3\%$ ).

#### Film structure

Figure 2a–b present representative cross-polarized light micrographs of cast film sections. The cast films exhibited spherulitic skin-core-type morphologies showing evidence of mixed  $\alpha/\beta$  spherulites and trans-crystalline growth in accordance with Fujiyama et al. [14] and Tamura et al. [15], [11]. Larger spherulites were observed in the core-layers while the spherulite size decreased gradually near the skin-layers, with a tendency of higher crystallinity and crystal grain size in the skin layer near the opposite side of chill roll (OCR) side. Characteristics of the initial spherulitic cast film morphology are of profound relevance for the morphology development of BOPP film [4], as upon biaxial stretching, the spherulites are deformed through a number of structural rearrangement processes into a highly-oriented fibrillar network structure [2], [16].

Optical analysis of the BOPP films (not shown) indicated significant differences in film translucency, with BOPP film haze increasing in proportion with cast film  $\beta$ -crystallinity. Further, optical analysis not only confirmed crater-like surface roughness on the BOPP film surfaces [15], [11], but also varying amounts of internal features within the film bulk. SEM-cross sectional imaging of the BOPP films, as exemplified in Figure 2c–d, revealed varying amounts of porosity and voids parallel to film surface, with the amount of voids/porosity increasing in proportion with the  $k_\beta$  of the corresponding cast film (Table 2). Mechanisms behind initial cavitation and elongation of voids by biaxial stretching in  $\beta$ -iPP films were recently discussed by Offord et al. [6], [10]—

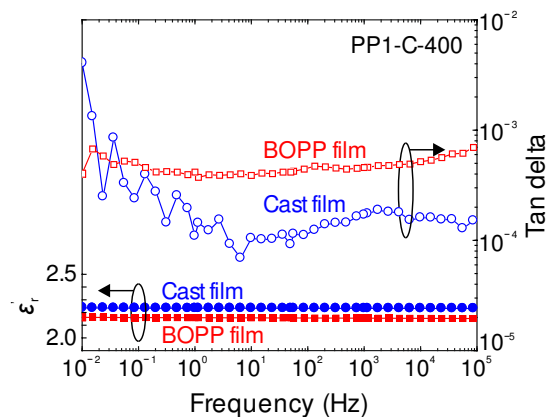
similar mechanisms are likely playing a role in the void formation for the mixed  $\alpha/\beta$ -phase iPP films studied here.

Figure 2e presents exemplifying optical profilometer height profiles of a PP1-B-400-5.6 specimen from the chill roll side (CR) and opposite side of chill roll (OCR). In accordance with Tamura et al. [15], [11] and Fujiyama et al. [17] the BOPP film surface topography and roughness on each film side were strongly related with  $\beta$ -form crystallinity and the spherulitic/trans-crystalline skin-core morphology of the each corresponding cast film. A variety of different surface morphologies were observed, ranging from very smooth surfaces (in particular the on the CR side) to rough and fibrillated surfaces consisting of crater-like surface structures.

### 3.2. Dielectric properties

#### Dielectric spectroscopy results

Dielectric spectroscopy results at the frequency of 1 kHz are given in Table 3. Figure 3 shows a comparison of real permittivity and dielectric loss of a PP1-C-400 cast film and a PP1-C-400-5.6 BOPP film as a function of frequency. For the cast films, the real permittivities



**Figure 3 –** Relative permittivity (real part) and dielectric loss of PP1-C-400 cast film and PP1-C-400-5.6 BOPP film.

**Table 3** – Dielectric spectroscopy and DC breakdown strength results. Real relative permittivity ( $\epsilon'_r$ ) and dielectric loss ( $\tan \delta$ ) are given at frequency of 1 kHz. For the large-area multi-breakdown performance, six sample films (81 cm<sup>2</sup> each) were measured, and breakdown fields  $E_{bd}$  at 5%, 63.2% and 95 % breakdown probability are given. For small-area single-breakdown performance, 20 samples were measured (1 cm<sup>2</sup> each), and 2-p Weibull parameters are given. Weibull  $\alpha$  corresponds to the breakdown field at 63.2% breakdown probability and the shape parameter  $\beta$  is inversely proportional to distribution homogeneity.

Code	Cast film		Biaxially stretched film						
	$\epsilon'_r$	$\tan \delta$ ( $\times 10^{-4}$ )	$\epsilon'_r$	$\tan \delta$ ( $\times 10^{-4}$ )	Large-area multi-BD (V/ $\mu\text{m}$ )			Small-area single-BD	
					$E_{bd}$ (5%)	$E_{bd}$ (63.2%)	$E_{bd}$ (95%)	$\alpha$ (V/ $\mu\text{m}$ )	$\beta$
PP1-A-500	2.24	1.90	2.16	5.69	566	680	728	669	14.7
PP1-B-400	2.24	1.73	1.83	3.88	317	466	537	515	17.5
PP1-C-400	2.24	1.70	2.12	4.69	621	754	810	812	17.8
PP1-C-200	2.12	1.64	2.14	4.19	360	699	765	717	22.2
PP2-A-500	2.23	1.82	1.83	4.50	493	622	678	633	15.3
PP2-B-400	2.20	1.66	1.82	3.63	334	450	554	462	16.2
PP2-C-400	2.21	1.57	2.12	3.97	642	753	798	794	27.4
PP2-C-200	2.11	1.47	1.93	4.51	428	623	741	709	21.4

(mean 2.20) and dielectric losses (mean  $1.69 \times 10^{-4}$ ) at 1 kHz were both consistent with typical values reported in literature [1]. A slight increase in  $\tan \delta$  at low frequencies was noticed for the cast films which could be attributed to reduced accuracy of the measurement equipment at low frequencies (for thick cast films) or interfacial polarization arising from the Al-foil electrodes. No notable difference in dielectric loss was observed between PP1 and PP2.

In contrary to the cast films, the BOPP films exhibited anomalous permittivities lower than those expected ( $<2.2$ ), see Table 3. The possibility of error in permittivity calculation arising from an error in film thickness was ruled out as this would have implied error of up to  $\sim 17\%$  in thickness measurement, which, given the manufacturer reported accuracy of 0.1  $\mu\text{m}$  for the thickness gauge, is not plausible. The accuracy of the film thickness measurement was later confirmed by sectional SEM-imaging. It is thus proposed that the observed decrease in BOPP film permittivity is attributable to the porosity/voids in BOPP film bulk (see the previous section)—similar decreases in permittivity with an increase in film porosity have previously been reported for diphasic foamed/cellular films of PP [18], polyethylene blends [19] and polyimides [20]. Interestingly, with an increase in film porosity, the dielectric losses should decrease in tandem with the permittivity [19]; such a trend was however not very clear for the BOPP films here. In contrary, the BOPP films showed slightly elevated dielectric losses in comparison to the corresponding cast films—to our current knowledge, this could be attributable substrate heating and/or other stresses occurring during the electrode deposition [21]. Nevertheless, the dielectric losses of the BOPP films (mean  $4.38 \times 10^{-4}$ ) are in line with the values reported elsewhere for BOPP films with evaporated Au-electrodes [22].

#### DC dielectric breakdown performance

Table 3 presents the DC large-area multi-breakdown and small-area single-breakdown results of the BOPP films. Breakdown data produced by the two methods were found to be in mutual agreement—the slightly higher dielectric strength indicated by the small-area single-breakdown method is attributable to the electrode area-

effect, as the probability of encountering weak points decreases when active area becomes smaller [9]. For some of the BOPP films, large-area multi-breakdown distributions showed deviation from a single 2-p Weibull distribution in the low probability region, similarly as previously presented in e.g. [1] for capacitor-grade BOPP films.

Comparing the different film variants manufactured by extruders A, B and C, large differences in breakdown performance were observed which can be linked to the morphological development during the cast film extrusion and biaxial stretching. An inverse relationship between cast film  $k_\beta$  and breakdown performance was observed, which is likely a manifestation of the microvoid/porosity formation associated with the  $\beta \rightarrow \alpha$  crystal transformation upon biaxial stretching of iPP cast film. An inverse trend between surface roughness and breakdown strength was also observed (not shown), with the results being consistent with those presented by Fujiyama et al. for a variety of surface-roughened BOPP films [23]. Further analysis and discussion on processing–structure–breakdown relationships is omitted from this paper and will be presented elsewhere [5].

## 4. Conclusions

Morphological development during cast film extrusion and biaxial orientation have profound effects on the film structure and dielectric integrity of BOPP films. For high-dielectric-performance films, careful optimization of the cast film crystalline structure is essential to avoid formation of structural defects due to  $\beta \rightarrow \alpha$  crystal transformation upon biaxial stretching. Results obtained on laboratory-scale films contribute to basic understanding on processing–structure–breakdown relationships in large-scale film manufacturing, however, differences in e.g. thermal and mechanical history between the two scales need to be carefully considered. Another parameter to consider is the BOPP film ageing under combined thermal and electrical stress [24].

## References

- [1] S. J. Laihonon, "Polypropylene: Morphology, Defects and Electrical Breakdown," Kungliga Tekniska Högskolan, PhD Thesis, 2005.

- [2] T. Lüpke, S. Dunger, J. Sänze, and H.-J. Radusch, "Sequential biaxial drawing of polypropylene films," *Polymer*, vol. 45, no. 20, pp. 6861–6872, Sep. 2004.
- [3] J. L. Nash, "Biaxially oriented polypropylene film in power capacitors," *Polym. Eng. Sci.*, vol. 28, no. 13, pp. 862–870, 1988.
- [4] M. Fujiyama, Y. Kawamura, T. Wakino, and T. Okamoto, "Study on rough-surface biaxially oriented polypropylene film. II. Influence of stretching conditions," *J. Appl. Polym. Sci.*, vol. 36, no. 5, pp. 995–1009, Aug. 1988.
- [5] I. Rytöluoto, A. Gitsas, S. Pasanen, and K. Lahti, "Effect of film structure and morphology on the dielectric breakdown characteristics of cast and biaxially oriented polypropylene films," *Eur. Polym. J.*, (Submitted), 2017.
- [6] G. T. Offord et al., "Porosity enhancement in  $\beta$  nucleated isotactic polypropylene stretched films by thermal annealing," *Polymer*, vol. 54, no. 10, pp. 2577–2589, 2013.
- [7] L. Capt, S. Rettenberger, H. Münstedt, and M. R. Kamal, "Simultaneous biaxial deformation behavior of isotactic polypropylene films," *Polym. Eng. Sci.*, vol. 43, no. 7, pp. 1428–1441, Jul. 2003.
- [8] I. Rytöluoto, K. Lahti, M. Karttunen, and M. Koponen, "Large-area dielectric breakdown performance of polymer films - Part I: Measurement method evaluation and statistical considerations on area-dependence," *IEEE Trans. Dielectr. Electr. Insul.*, vol. 22, no. 2, pp. 689–700, 2015.
- [9] I. Rytöluoto, "Large-Area Multi-Breakdown Characterization of Polymer Films: A New Approach for Establishing Structure–Processing–Breakdown Relationships in Capacitor Dielectrics," Tampere University of Technology, PhD Thesis, 2016.
- [10] G. T. Offord, S. R. Armstrong, B. D. Freeman, E. Baer, A. Hiltner, and D. R. Paul, "Influence of processing strategies on porosity and permeability of  $\beta$  nucleated isotactic polypropylene stretched films," *Polymer*, vol. 54, no. 11, pp. 2796–2807, May 2013.
- [11] S. Tamura, K. Ohta, and T. Kanai, "Study of crater structure formation on the surface of biaxially oriented polypropylene film," *J. Appl. Polym. Sci.*, vol. 124, no. 4, pp. 2725–2735, May 2012.
- [12] L. Capt, "Simultaneous biaxial stretching of isotactic polypropylene films in the partly molten state," McGill University, PhD Thesis, 2003.
- [13] F. J. Díez et al., "Influence of the stretching in the crystallinity of biaxially oriented polypropylene (BOPP) films," *J. Therm. Anal. Calorim.*, vol. 81, no. 1, pp. 21–25, 2005.
- [14] M. Fujiyama, Y. Kawamura, T. Wakino, and T. Okamoto, "Study on rough-surface biaxially oriented polypropylene film. VI. Roughening by laminated cast sheet," *J. Appl. Polym. Sci.*, vol. 36, no. 5, pp. 1049–1059, Aug. 1988.
- [15] S. Tamura, K. Takino, T. Yamada, and T. Kanai, "Crater formation mechanism on the surface of a biaxially oriented polypropylene film," *J. Appl. Polym. Sci.*, vol. 126, no. S2, pp. 449–456, 2012.
- [16] H. Y. Nie, M. J. Walzak, and N. S. McIntyre, "Draw-ratio-dependent morphology of biaxially oriented polypropylene films as determined by atomic force microscopy," *Polymer*, vol. 41, no. 6, pp. 2213–2218, 2000.
- [17] M. Fujiyama, Y. Kawamura, T. Wakino, and T. Okamoto, "Study on rough-surface biaxially oriented polypropylene film. I. Formation of  $\beta$ -form crystals in sheet cast with T-die extruder," *J. Appl. Polym. Sci.*, vol. 36, no. 5, pp. 985–993, Aug. 1988.
- [18] R. Schwodiauer et al., "Preparation and characterization of novel piezoelectric and pyroelectric polymer electrets," *IEEE Trans. Dielectr. Electr. Insul.*, vol. 7, no. 4, pp. 578–586, 2000.
- [19] M. Strååt, I. Chmutin, and A. Boldizar, "Dielectric Properties of Polyethylene Foams at Medium and High Frequencies," in *Transactions of the Nordic Rheology Society*, 2010, pp. 107–116.
- [20] B. Krause, G.-H. Koops, N. F. A. van der Vegt, M. Wessling, M. Wübberhorst, and J. van Turnhout, "Ultralow-k Dielectrics Made by Supercritical Foaming of Thin Polymer Films," *Adv. Mater.*, vol. 14, no. 15, p. 1041, Aug. 2002.
- [21] A. Kahouli et al., "Structure effect of thin film polypropylene view by dielectric spectroscopy and X-ray diffraction: Application to dry type power capacitors," *J. Appl. Polym. Sci.*, p. 42602, 2015.
- [22] N. Zhang, J. Ho, J. Runt, and S. Zhang, "Light weight high temperature polymer film capacitors with dielectric loss lower than polypropylene," *J. Mater. Sci. Mater. Electron.*, pp. 1–6, 2015.
- [23] M. Fujiyama, Y. Kawamura, T. Wakino, and T. Okamoto, "Study on rough-surface biaxially oriented polypropylene film. V. Analysis and control of roughness," *J. Appl. Polym. Sci.*, vol. 36, no. 5, pp. 1035–1048, Aug. 1988.
- [24] M. Ritämäki, I. Rytöluoto, K. Lahti, T. Vestberg, S. Pasanen, and T. Flyktman, "Large-Area Approach to Evaluate DC Electro-Thermal Ageing Behavior of BOPP Thin Films for Capacitor Insulation Systems," *IEEE Trans. Dielectr. Electr. Insul.*, vol. 24, no. 2, pp. 826–836, 2017.